Precapillary sphincters control cerebral blood flow

Søren Grubb[1]*, Changsi Cai[1]*, Bjørn O. Hald[1], Lila Khennouf[1,2], Jonas Fordsmann[1], Reena Murmu[1], Aske G. K. Jensen[1,3], Stefan Zambach[1] & Martin Lauritzen[1]

[1]Department of Neuroscience, Faculty of Health Sciences, University of Copenhagen, DK-2200 Copenhagen N, Denmark. [2]Department of Neuroscience, Physiology and Pharmacology, University College London, Gower Street, London, WC1E 6BT, UK. [3]Department of Neurosciences, University of California, San Diego, CA 92093, USA

*These authors contributed equally to this work

Abstract

Active nerve cells produce and release vasodilators that increase their energy supply by dilating local blood vessels, a mechanism termed neurovascular coupling, which is the basis of the BOLD (blood-oxygen-level-dependent) functional neuroimaging signals. We here reveal a unique mechanism for cerebral blood flow control, a precapillary sphincter at the transition between the penetrating arteriole and the first capillary that links blood flow in capillaries to the arteriolar inflow. Large NG2-positive cells, containing smooth muscle actin, encircle the sphincters and rises in nerve cell activity cause astrocyte and neuronal Ca^{2+} rises that correlate to dilation and shortening of the sphincter concomitant with substantial increases in the RBC flux. Global ischemia and cortical spreading depolarization constrict sphincters and cause vascular trapping of blood cells. These results reveal precapillary sphincters as bottlenecks for brain capillary blood flow.

Introduction

Neurovascular coupling (NVC) is the signalling mechanism that links neuronal activity to local increases in

cerebral blood flow[1]. Ca^{2+} rises in neurons and astrocytes trigger release of vasoactive compounds that dilate

capillaries and penetrating arterioles, which in turn increases local blood flow. The activity-induced rises in

blood flow are based on coordinated changes in the diameters of arterioles and capillaries which in turn are

regulated by Ca^{2+} fluctuations within the vascular smooth muscle that circumscribe arterioles and the

pericytes which ensheath capillaries close to the penetrating arteriole[2–5]. Intracortical arterioles branch into

the capillary networks that supply the cortical layers with oxygen and glucose[6]. It is unclear, however, how

the organization of blood supply can ensure a roughly equal perfusion of capillary networks at different

cortical depths. The organization encounters two competing obligations: preservation of perfusion pressure

in the penetrating arteriole along the entire cortical depth, which is essential for adequate blood flow to all

layers, yet the brain tissue must be shielded from the mechanical impact of blood pressure rises. Here, we

reveal the structure and function of brain precapillary sphincters, which may serve exactly these two

purposes: capillary protection from systolic pressure spikes and preservation of perfusion pressure despite

capillary branching from the penetrating arteriole. We characterized precapillary sphincters as mural cells

34   encircling an indentation of blood vessels exactly where capillaries branch off from penetrating arterioles.

35   The sphincter cells had a bulbous soma similar to brain pericytes, contained α-smooth muscle actin and were

36   ensheathed by structural proteins. Precapillary sphincters were present at most but not all proximal capillary

37   branches of penetrating arterioles (PA) and with a decrease in occurrence from upper to lower cortical layers,

38   an ideal position to facilitate a balanced perfusion pressure along the PA and for brain protection against

39   arterial pressure pulsations. While precapillary sphincters have been known for almost a century[7], their

40   existence in all vascular beds except for the mesentery[8–10] remains controversial[11,12]. This paper provides

41   unequivocal structural and functional evidence for brain precapillary sphincters and examines their role in

42   neurovascular coupling and in pathology during cortical spreading depolarization (CSD) and global ischemia

43   following cardiac arrest.

Results

46   ## Precapillary sphincters mainly locate to the proximal branch-points of penetrating arterioles

47   We identified precapillary sphincters in mice expressing dsRed under the NG2 promoter as lobular dsRed-

48   positive cells encircling an indentation of the vessel lumen at PA branch-points (Fig. 1a). Precapillary

49   sphincters were most often followed by a distention of the lumen, which we denoted "the bulb". The dsRed

50   signal from the precapillary sphincter was usually brighter than the dsRed signals from other mural cells on

51   the PAs and 1st order capillaries indicating high NG2-expression. However, the dsRed signal from the bulb

52   region was low compared to the rest of the 1st order capillary (Fig. 1a,b,d), which suggested low pericyte

53   coverage. We could show that precapillary sphincters and bulbs were not only present in anesthetized mice,

54   but also in awake mice with chronic cranial windows *in vivo* (Fig. 1c and Extended data Fig. 3, n = 4) and in

55   anesthetized NG2-dsRed mice with thinned skull over the barrel cortex *in vivo* (Fig. 1b, Extended data Fig. 2

56   and Supplementary video 1, n = 3). *Ex vivo* studies revealed that the NG2-positive cells encircling the

57   precapillary sphincter were individual cells encompassing the sphincter at the branchpoint and not processes

58   of mural cells extending from the PA (Fig. 1d). DAPI stain of coronal brain slices, revealed that penetrating

59   arterioles were covered with smooth muscle/pericyte hybrids (Fig. 1e), indicating a continuum of mural cell

60   cyto-architecture from pial arterioles to 3rd order capillaries as previously described[13–15].
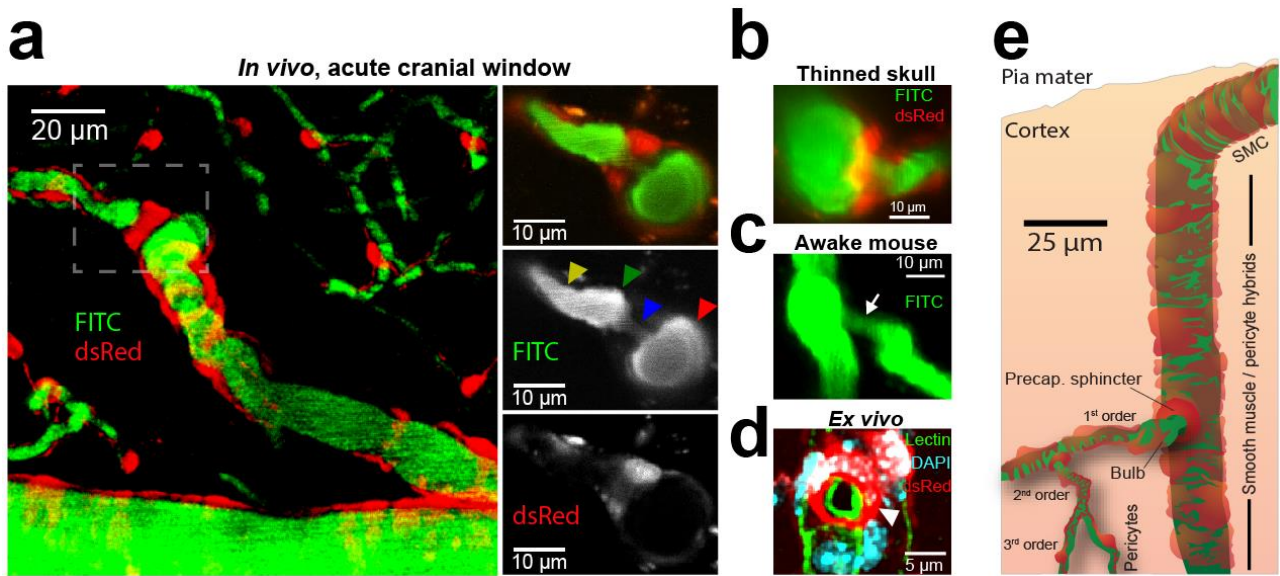
61

62   Figure 1 | **Precapillary sphincters are found on the proximal branches of penetrating arterioles. a**, *Left*
63   *panel*: Maximal intensity projected *in vivo* two-photon laser scanning microscopy image of an NG2-dsRed mouse barrel cortex. An
64   indentation of capillary lumen is observed at the branching of the penetrating arteriole (PA)and is encircled by bright dsRed cell(s)
65   (dashed insert). This structure is denoted a precapillary sphincter. Immediately after the sphincter a sparsely dsRed-labeled distention
66   of the capillary lumen is observed, which we refer to as "the bulb". *Right panels*: Single z-plane showing overlay, FITC-channel, and
67   dsRed channel of the dashed insert. Arrows indicate the PA (red), sphincter (blue), bulb (green) and 1st order capillary (yellow). **b-d**,
68   Local TPLSM projections of precapillary sphincters in cortex of: **b**, a thinned skull mouse *in vivo*, **c**, an awake mouse harboring a
69   chronic cranial window *in vivo*. White arrows mark the precapillary sphincter, and **d:** an *ex vivo* coronal slice of a FITC-conjugated
70   lectin (green) stained NG2-dsRed mouse (red) with DAPI staining (blue) of nuclei. The precapillary sphincter cell nucleus is arched,
71   as it follows the cell shape. **e**, Schematic of a PA with a precapillary sphincter at the proximal branch-point based on *ex vivo* data.
72   The morphology and location of NG2-dsRed positive cells on the vascular tree are indicated.

73

74   Having established the structure of precapillary sphincters, we examined their occurrence and localization

75   within the cortical vascular network. In keeping with the work of Duvernoy et al.[6], we identified a range of

76   PA subtypes (Fig. 2b) that differed in size, branching pattern and cortical penetration. Precapillary sphincters

77   were predominantly localized to the upper layers of the cortex (Fig. 2c) and were mainly observed at

78   proximal PA branch-points (Fig. 2d) of relatively large PAs branching into relatively large 1st order

79   capillaries (Fig. 2e,f). As larger proximal vessels carry higher blood pressures than downstream vessels, this

80   localization indicated that sphincters contributed to pressure distribution. The bulb usually succeeded a

81   sphincter, but was less prevalent and did not display the same positive correlation with the diameter of the 1st

82   order capillary as the sphincter (Fig. 2e), i.e. bulbs were observed when the PA diameter was large compared

83   to the 1st order capillary (Fig. 2f). For branches positive for a precapillary sphincter, the average diameter of

84   the PA was 11.4 ± 0.6 µm, the precapillary sphincter was 3.4 ± 0.2 µm, the bulb was 5.8 ± 0.2 µm, and the

85   1st order capillary was 5.3 ± 0.2 µm (mean ± SEM). As per Poiseuille's law (adjusted for flow velocity, Fig.

86   2g), a lumen diameter around 3-4 µm is precisely at the border of very high flow resistance, providing an

87   effective means of changing the pressure drop per unit length. We conclude that precapillary sphincter

88   complexes (sphincter *and* bulb) 1) are characterized by an indentation of lumen at the branch-point encircled

89   by a sphincter cell usually followed by a distention (the bulb) and 2) are common at proximal PA branch-

90   points, predominantly at larger PAs in the mouse cortex.

91
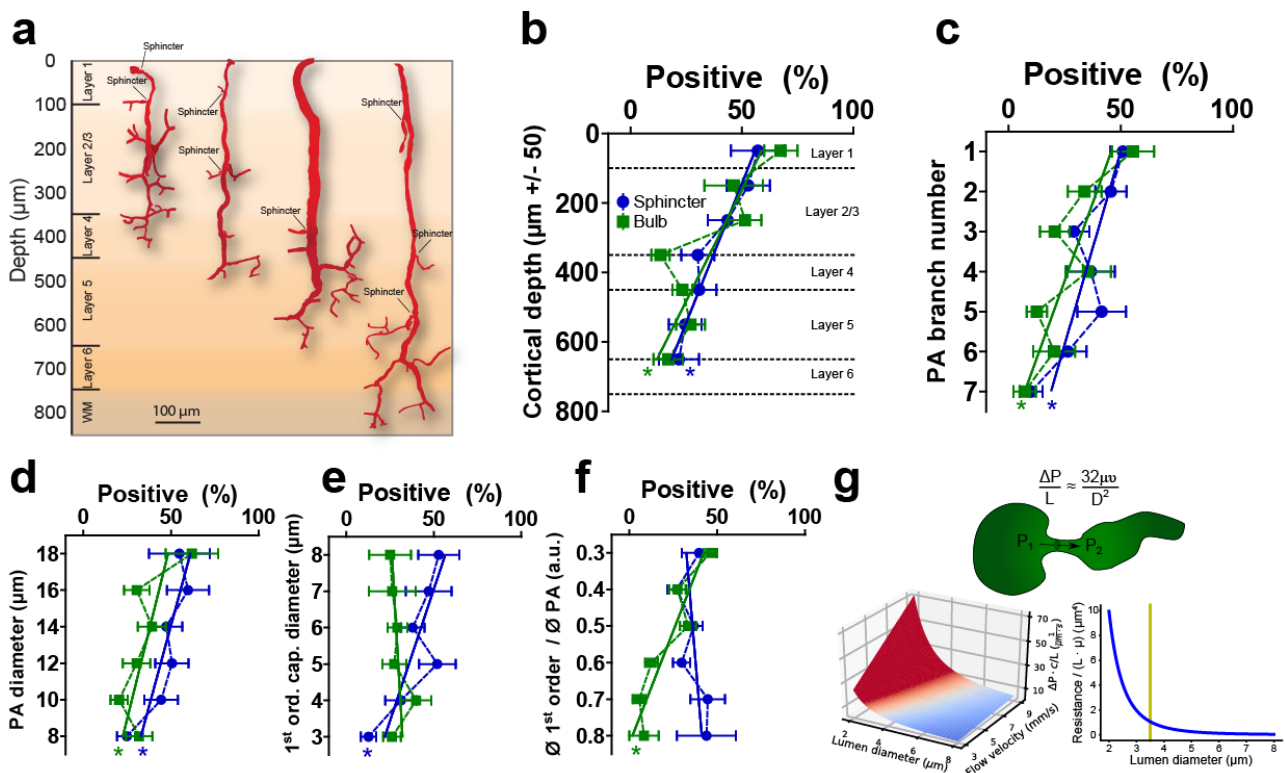
Figure 2 | **Presence, location, and biophysics of cortical precapillary sphincters suggest a function in pressure equalization across the PA. a**, Representatives of four PA subtypes[6] reaching different cortical layers based on *ex vivo* data. Precapillary sphincters are found at varying depths. **b-f,** Dependency of the presence and location of precapillary sphincters and bulbs (binned quantification) on various parameters. Criteria of a positive presence of sphincter or bulb at a branch point: sphincter <0.8 and bulb >1.25 times the diameter of a 1st order capillary, N = 6-8 mice, ±SEM, linear regression, * = slope deviates significantly from 0. **b,** dependency on cortical depth (bin size 100 µm). **c**, dependency on PA branch number (counting from the proximal end). **d,** dependency on PA diameter (bin size 2 µm). **e,** dependency on 1st order capillary diameter (bin size 1 µm). **f,** dependency on 1st order cap / PA diameter ratios (bin sizes as in d and e). **g**, *Top panel:* Illustration of a pressure drop across a precapillary sphincter and a modified expression of Poiseuille's law (ΔP: pressure difference, L: unit length, µ: viscosity, υ: flow velocity). *Lower left*: Graphical illustration of Poiseuille's law showing how the pressure difference times viscosity per unit length depends on the cylindrical lumen diameter and flow velocity. Note how the pressure difference increases with lumen diameters below ~ 4µm. *Lower right*: An

103 equivalent representation of how flow resistance per unit length and viscosity depends on lumen diameter according to Poiseuille's
104 law.

105

Precapillary sphincters actively regulate capillary blood flow

107 Having established the occurrence and morphology of precapillary sphincter complexes, we examined their

108 role in blood flow regulation. First, we confirmed expression of α-smooth muscle actin (α-SMA) within the

109 precapillary sphincter cell in coronal slices of NG2-dsRed mice (Fig. 3a, vascular lumen and cell nuclei co-

110 stained using lectin and DAPI, respectively. See also Extended data Fig. 4 and Supplementary video 2).

111 Next, we analyzed the vasomotor responses of the PA, precapillary sphincter, bulb, and 1st order capillary

112 vessel segments in response to electrical whisker pad stimulation in an *in vivo* two-photon setup (Extended

113 data Fig. 1). Careful placing of linear regions of interest (ROIs) in hyperstacks of two-photon images were

114 used to avoid inter-segmental interference in diameter calculations before and during whisker stimulation

115 (Fig. 3b-c and Supplementary video 3). Precapillary sphincters dilated during stimulation followed by a post-

116 stimulus constriction, denoted the post-stimulus undershoot at 20-30 s after stimulation. Four-dimensional

117 hyperstack imaging allowed us to confirm that the undershoot was not an artifact of drift in the z-axis.

118 Relative diameter changes at the sphincter were significantly higher compared to the PA and the rest of the

119 1st order capillary during both dilation (33.75±4.08%, Fig. 3e and Extended data Table 1) and undershoot (-

120 12.40±2.10%, Fig. 3f and Extended data Table 1). To estimate the corresponding changes in flow resistance

121 per unit length, we applied Poiseuille's law at baseline, maximal dilation, and maximal undershoot (Fig. 3g-

122 i). The flow resistance of the sphincter at rest was significantly higher compared to the other segments and

123 decreased significantly more (65.9% decrease, Fig. 3h) during dilation as compared to all other segments

124 (40.8% for the 1st order capillary, Fig. 3h). During the post-stimulus undershoot, flow resistance increased by

125 80.2% at the sphincter (Fig. 3i), which highlights the sensitivity of flow resistance to sphincter constriction

126 and underscores the strategic control of flow resistance at the sphincter due to the power law relationship

127 between diameter and flow resistance (Fig. 2g). Moreover, we observed that the length of precapillary

128 sphincters decreased during stimulation and increased during undershoot (Extended data Fig. 5). According

129 to Poiseuille's law, shortening of the sphincter decreases the absolute flow resistance across the precapillary

130   sphincter complex and vice versa, i.e. further reducing the pressure drop across the sphincter during

131   functional dilation and increasing the pressure drop during the undershoot. We examined intracellular Ca^{2+}

132   dynamics in neuronal somas and astrocytic end-feet enwrapping the vessel segments (Extended data Fig. 6).

133   Neuronal somas and astrocytic end-feet responded with increases in intracellular Ca^{2+} upon whisker pad

134   stimulation and in the undershoot phase (Extended data Fig. 6b-e). The fraction of ROIs responding was

135   similar during dilation and undershoot and independent of the location of the end-feet on the vascular three

136   (Extended data Fig. 6f).

137   We next examined the correlation between red blood cell flux and diameter changes in response to whisker

138   pad stimulation (Fig. 3j-m). RBC velocity fluctuated in synchrony with systolic and diastolic oscillations in

139   arterial blood pressure (Fig. 3j,k). At rest, the average RBC velocity through precapillary sphincters was

140   8.7 ± 0.6 mm/s (Fig 3l), significantly higher than for the bulb (3.6 ± 0.6 mm/s) and the 1st order capillary

141   (4.7 ± 0.6 mm/s), but correlated to the relative differences in resting diameters of the vessel segments. As

142   shown in Fig. 2G, high RBC velocity through the narrow lumen of the precapillary sphincter amplifies the

143   reduction of pressure across the sphincter due to high shear and thereby contributes to the protection of

144   downstream capillaries from high pressures in large proximal PAs. From the baseline measures, the pressure

145   drop per unit length is 4 times larger in the sphincter compared to the 1st order capillary, assuming that RBC

146   velocity and fluid velocity are roughly equal, see Fig. 2g. During whisker stimulation (Fig. 3l), both diameter

147   and RBC velocity increased in each segment but significantly more at the precapillary sphincter than the 1st

148   order capillary (Fig. 3m). The flux of RBC's through the precapillary sphincter complex increased by 25%

149   from baseline to peak stimulation (mean flux rose from 543 ± 25 to 679 ± 50 cells per second, Fig. 3l). Given

150   the high RBC velocity, a baseline flux in the first order capillary of around 550 cells per second is not

151   surprising (see Extended data calculation 1). The sphincter, however, retained a dampening effect on

152   pressure during peak stimulation, where the pressure drop per unit length was 3 times larger at the sphincter

153   compared to the 1st order capillary. RBC velocity and flux returned to baseline at 20-30s after end of

154   stimulation (Fig. 3l), concurrent with the post-stimulus undershoot (Fig. 3c,f) [17],[16]. Before, during, and after

155   whisker stimulation, we observed fluxes of single RBCs through the precapillary sphincter into the 1st order

156   capillary, which may optimize oxygen delivery to the tissue (Supplementary video 5). Collectively, our data

157   suggest that the sphincter complex 1) protects downstream capillaries from blood pressure peaks in the

158   proximal PAs, 2) actively regulates local diameter and RBC flux during functional stimulation, and 3)

159   equalizes the distribution of RBCs entering the upper and lower cortical layers.

160
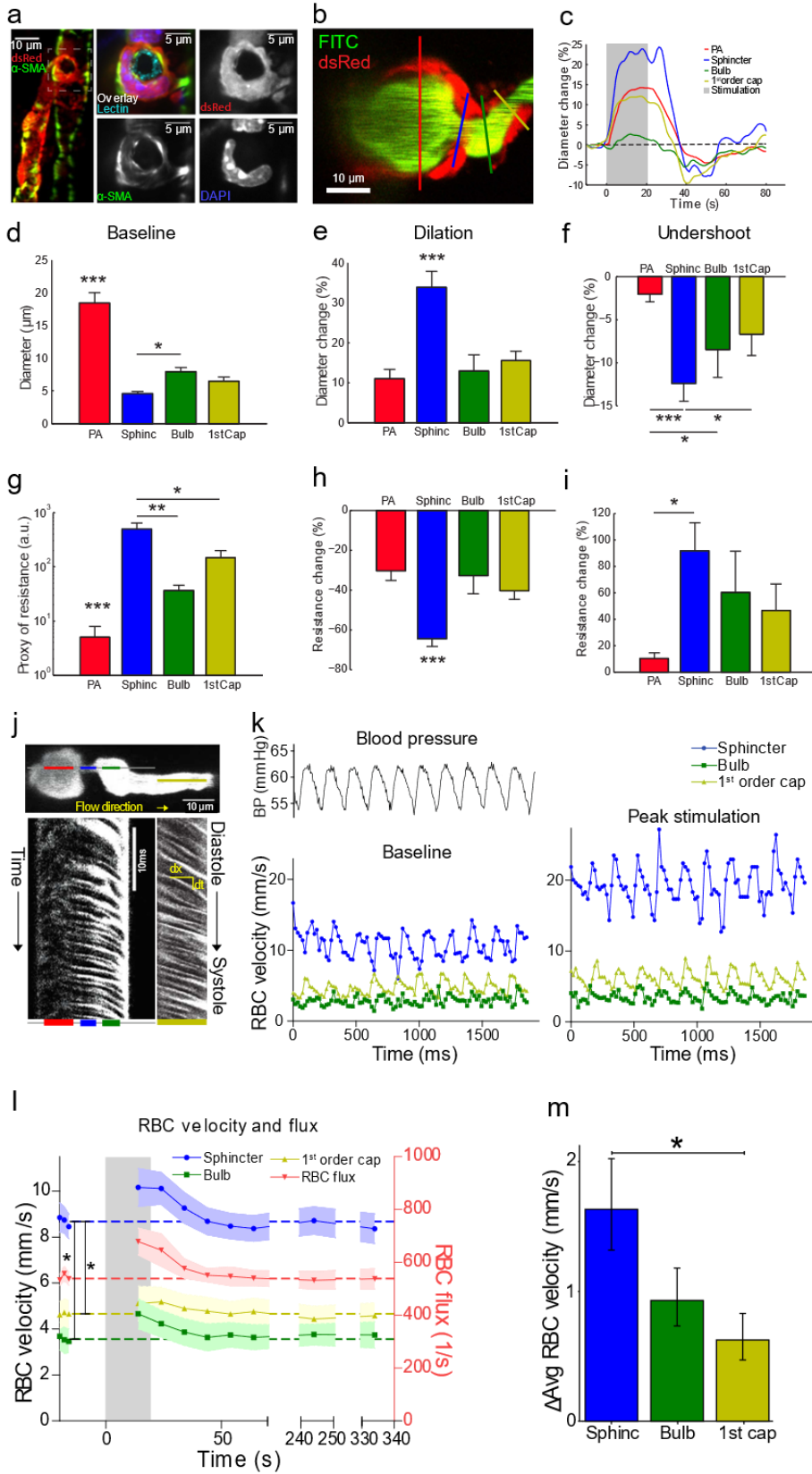
Figure 3 | **Precapillary sphincters are actively regulating blood flow upon functional stimulation. a,** *Ex*
vivo coronal slices of a FITC-lectin stained NG2-dsRed mouse immunostained for α-SMA. *Left panel*: Maximal projection of a PA

163 with a precapillary sphincter at the 1st order capillary branchpoint, marked area is shown in right panels. *Right panels*: Local maximal
164 intensity projections of the precapillary sphincter region of either dsRed, α-SMA, DAPI, or all channels including FITC-lectin
165 overlayed. **b-i**, *In vivo* whisker pad stimulation experiments (anesthetized NG2-dsRed mice) using maximal intensity projected 4D
166 data obtained by two-photon microscopy. **b**, Maximal intensity projection of a PA branchpoint where the colored lines indicate the
167 ROIs for diameter measurements for the vessel segments PA (red), precapillary sphincter (blue), bulb (green) and 1. order capillary
168 (yellow). **c**, Representative time series of relative diameter dynamics in each vessel segment upon 20s of 5 Hz whisker pad
169 stimulation (grey bar, start at time zero). **d**, Summary of baseline diameters (absolute values). **e**, Summary of peak diameter change
170 upon whisker pad stimulation. **f**, Summary of peak undershoot phase after whisker pad stimulation. **g**, A proxy of flow resistance at
171 baseline estimated using Poiseuille's law. **h**, Relative change in flow resistance at peak dilation during stimulation. **i**, Relative change
172 in flow resistance during the post-stimulation undershoot. **j-m**, RBC velocity and flux estimation. **j**, Resonance scanning allows for
173 rapid repetitive line-scans in a single z-plane (upper panel). In the resulting space-time maps (lower panel), individual cells display in
174 black with an angle proportional to the cell velocity. Red, blue, green and yellow lines indicate the regions of the line-scans deriving
175 from the PA, sphincter, bulb, and the 1st order capillary (1st order capillaries were mostly scanned in consecutive experiment). **k**,
176 Fluctuations in femoral artery blood pressure (left upper panel) and RBC velocity (left lower panel) correlated. During whisker pad
177 stimulation (right panel), RBC velocity increased. **l**, Time series of RBC velocities and flux during whisker pad stimulation. RBC
178 velocity at the precapillary sphincter was significantly higher than the bulb and 1st order capillary at baseline and peaked around 10s
179 after stimulation before returning to baseline. **m**, Summary of the difference between maximal and baseline RBC velocity during
180 whisker stimulation. The Kruskal-Wallis test was used in d, g, and i to reveal differences among vessel segments followed by a
181 Wilcoxon rank-sum test (with Holm's p-value adjustment) for pairwise comparisons. LME models were used in e, f, h, and m to test
182 for difference among segments followed by Tukey post hoc tests for pairwise comparisons. In m, the LME analysis was performed
183 on log-transformed data to ensure homoskedasticity.

184

185 ## Passive structural elements around the precapillary sphincter support the bottleneck function

186 The presence of a contractile sphincter-encircling pericyte, supports the notion of active regulation of the

187 diameter at the precapillary sphincter. The indentation of the sphincter, however, might also be supported by

188 passive elements to optimize the force-length relationship[17]. We therefore investigated whether passive

189 structural elements constrained dilation at the sphincter by injecting papaverine (10 mM), a strong

190 vasodilator, close to the sphincter (Fig. 4a-c). Papaverine blocks the contractility of the vascular smooth

191 muscle cells, and by inference pericytes, by inhibiting vascular phosphodiesterases[18] and calcium channels[19].

192 Under these conditions, passive structural elements of the vessel become the main factors that stabilize the

193 vessel wall in face of the unaffected transmural pressure. Both before and after papaverine injection, the

194 lumen diameter of the sphincter was significantly smaller than for the bulb and 1st order capillary (Fig. 4c).

195 Yet, the sphincter showed a significantly larger dilation in absolute and relative terms, as compared to the 1st

196 order capillary. Structural evidence of passive connective tissue was established by staining coronal slices of

197 NG2-dsRed mice with either a collagen α1 type I (COL1A1) antibody or Alexa633 hydrazide, a marker of

198 elastin[20]. Elastin was observed in the tunica intima of penetrating arterioles and at the precapillary sphincter,

199 but not at the level of 1st order capillaries (Fig. 4d). Collagen α1 type I staining was observed in the tunica

200 externa of arterioles, precapillary sphincters, capillaries (Fig. 4e), and venules. Thus, common structural

201 proteins ensheathed the precapillary sphincter. The data indicates that the active sphincter is supported by

202 passive structural elements that assist the active pericyte in protecting soft brain tissue against pressure

203 increases produced by dilation of the PA.
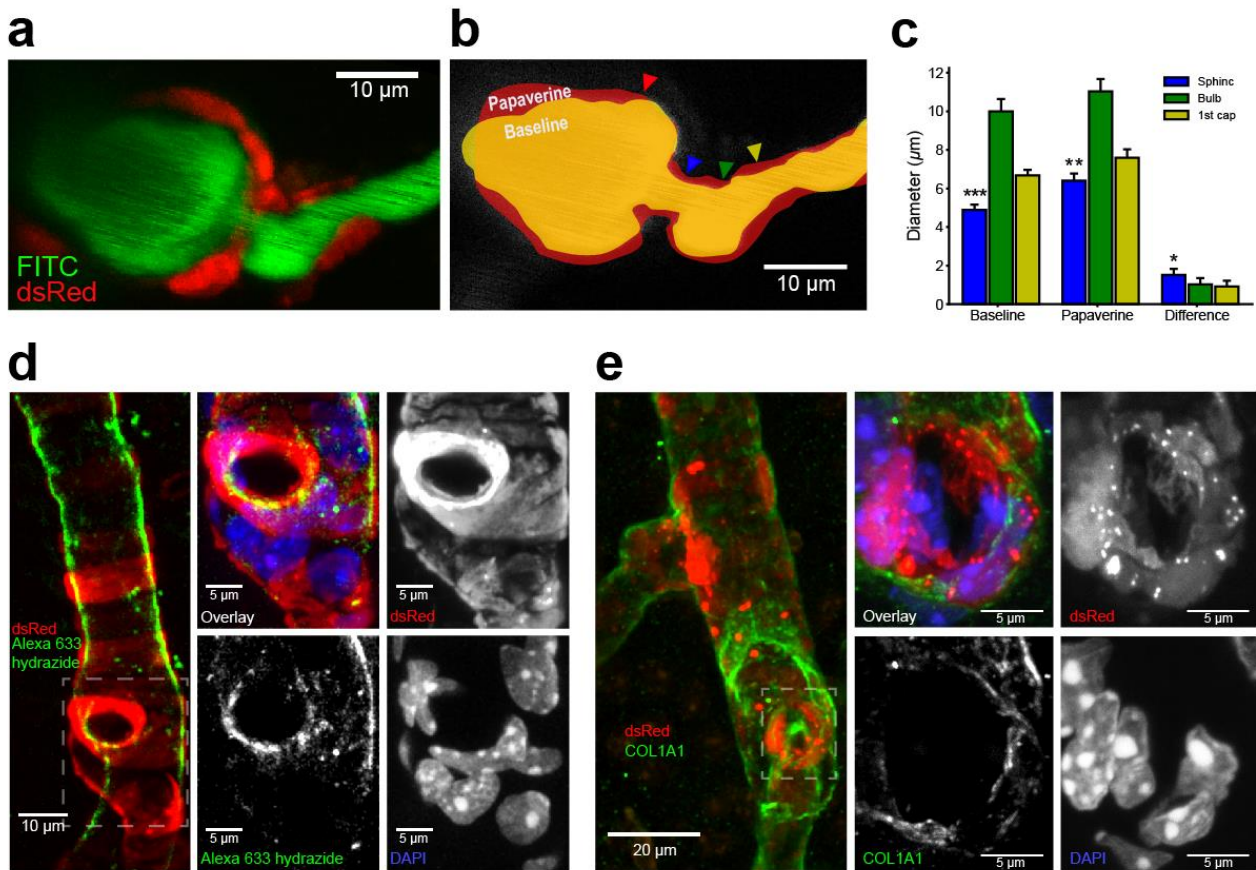
205 Figure 4 | **Precapillary sphincters harbor passive structural elements that delimit capacity for vasodilation. a-d**, Papaverine (10
206 mM) was locally injected into the vicinity of precapillary sphincters to dilate the nearby vasculature. **a**, Representative maximal
207 intensity projection of an NG2-dsRed mouse PA branch-point. **b**, Schematic showing the papaverine induced dilation (red) below an
208 outline of the vessel lumen at baseline (yellow). ROI locations of individual vessel segments are marked by colored arrows. **c**,
209 Absolute diameters of vessel segments 1) at baseline, 2) after papaverine addition, and 3) the difference before and after papaverine
210 addition. The baseline dataset was analyzed using the Kruskal-Wallis test followed by a Wilcoxon rank-sum test (with Holm's p-
211 value adjustment) for pairwise comparisons. The papaverine and difference datasets were analyzed using LME models followed by
212 Tukey post hoc tests for pairwise comparisons. **d**, Maximal intensity projections of coronal slices of NG2-dsRed mice stained with
213 Alexa633 hydrazide and DAPI. *Left panel*: 20x magnification of a penetrating arteriole with a precapillary sphincter at the
214 branchpoint. *Right panels*: 63x magnification of the precapillary sphincter and 1st order capillary. Alexa633 hydrazide staining is
215 strong at the sphincter but absent in the 1st order capillary. **e**, Maximal intensity projections of coronal slices of NG2-dsRed mice
216 stained with COL1A1 antibody and DAPI. *Left panel*: 20x magnification of a penetrating arteriole with two branches. *Right panels*:
217 63x magnification of the precapillary sphincter at the lower branch.

219   ## The precapillary sphincter in cortical spreading depolarization and during global ischemia.

220   In the healthy mice considered so far, precapillary sphincter complexes displayed an active role in regulation

221   and protection of downstream capillary blood flow (Fig. 3,4). As observed for the undershoot (Fig. 3f,i), the

222   flow resistance of the sphincter may increase strongly under physiological conditions (Fig. 2g). This

223   observation prompted the question of whether sphincters constrict in brain pathology. Hence, we investigated

224   sphincter dynamics during cortical spreading depolarization (CSD) waves that are caused by disrupted brain

225   ion homeostasis and known to cause prolonged vasoconstriction[4]. Microinjection of 0.5 M potassium acetate

226   in the posterior part of the somatosensory cortex elicited CSD that triggered a triphasic sequence of changes

227   the in the diameter and flow of cortical blood vessels consisting of: (I) a brief initial constriction followed by

228   (II) a longer-lasting dilation and (III) a prolonged vasoconstriction (Fig. 5a-c, supplementary video 6).

229   Whereas the maximal constriction relative to baseline in phase I was similar among vessel segments, the

230   maximal relative dilation of the precapillary sphincter in phase II was greater than for the bulb and the 1st

231   order capillary (Fig. 5d, 39±8%, vs. 22±3 and 21±4%) but not different from maximal dilation during

232   whisker pad stimulation (34±4%, Fig. 3e) or local injection of papaverine (32±8%, Fig. 4c). During phase

233   III, the precapillary sphincter constricted more (26.2%) than the PA and the bulb and generated a doubling in

234   flow resistance (Fig. 5e). This was occasionally accompanied by transitory entrapment of RBCs at the

235   sphincter that occluded the 1st order capillary (Supplementary video 4), consistent with the high increase in

236   flow resistance. These results show that the sphincter constricts markedly in CSD, which is likely to be

237   highly important for the associated long lasting decreases in cortical blood flow that follows CSD[21].

238

239
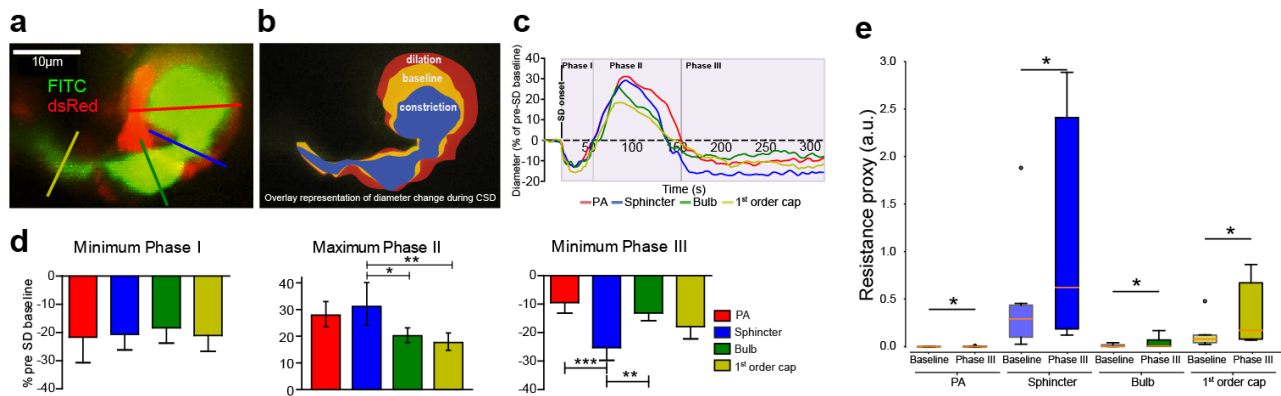
Figure 5 | **a-d**, **Precapillary sphincters are vulnerable to conditions of general constriction.** Cortical spreading depolarization was elicited in the posterior part of the somatosensory cortex by microinjection of potassium acetate during imaging of the precapillary sphincter. **a**, Representative maximal intensity projection of a FITC-dextran loaded NG2-dsRed mouse at a precapillary sphincter. Colored lines mark the ROIs for diameter measures. **b**, Overlaid outlines of baseline (yellow), phase II dilation (red) and phase III constriction (blue). **c**, Representative time series of diameter changes within vessel segments during the three phases of CSD. **d**, Summaries of maximal diameter changes within vessel segments during phase I, II and III of the CSD. During phase II, the PA and sphincter dilated significantly more than the 1st order capillary. During phase III, the sphincter constricted significantly more than the PA and the bulb. Datasets were analyzed via LME models followed by Tukey post hoc tests for pairwise comparisons (Phase II data was log-transformed to ensure homoskedasticity). **e**, Boxplot summary of the estimated flow resistances at vessel segments during baseline and phase III of CSD. Paired Wilcoxon signed rank tests were used to establish difference ($p < 0.05$) before and during CSD phase III.

We also examined the vulnerability of the precapillary sphincter to global ischemia induced by cardiac arrest

(Fig. 6). Cardiac arrest caused an immediate loss of blood pressure and an initial $26\pm7\%$ mean drop in lumen

diameter within the first 2 minutes (Fig. 6b,c, n = 7), which was most prominent at the bulb. Over the

subsequent 30 minutes we observed vasoconstriction of the cerebral microvessels that occurred with

important differences in time delay. The sphincter remained relatively unchanged for the first ~14min,

whereas the PA and 1st order capillary showed a steady reduction in diameter. After 14-20 minutes, we

observed an accelerated constriction spreading from the 1st order capillaries towards the PA and along the PA

towards the brain surface (Supplementary video 7). The precapillary sphincter collapsed at a rate of

0.23 ± 0.03 µm min^{-1} (Fig 6c, phase II). The collapse of the sphincter was complete after ~25min and caused

an extreme increase in flow resistance (Fig 6d, phase III) that essentially occluded entry of RBCs into the

capillary networks. Concurrent with the collapse of the vessel lumen, we observed a swelling of astrocytic

end-feet and vasculature-associated astrocyte soma (Supplementary video 7).

263
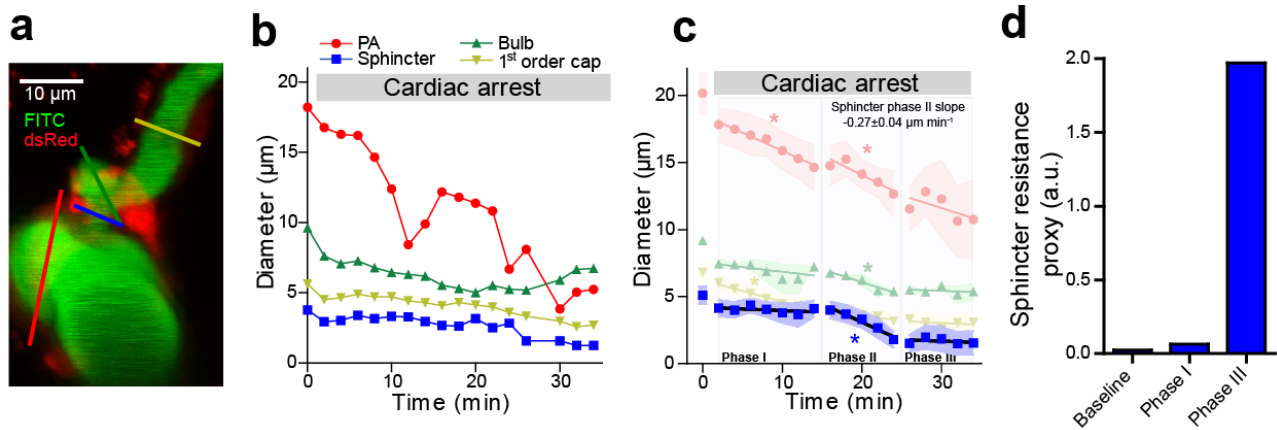
Figure 6 | **The integrity of precapillary sphincters represents a vulnerable site to prolonged ischemia.** Cardiac arrest and global ischemia was elicited by intravenous injection of pentobarbital (50 µl of a mix of 200 mg/mL pentobarbital and 20mg/mL lidocaine) during imaging of the precapillary sphincter. **a**, Representative maximal intensity projection of a FITC-dextran loaded NG2-dsRed mouse. Color coded lines mark the ROIs for repeated diameters measures before and after cardiac arrest. **b**, Representative time series of diameter changes at vessel segments during cardiac arrest. The initial diameter decrease is due to the loss of blood pressure. **c**, Summary time series of diameter changes after cardiac arrest. Three phases were constructed based on the dynamics of the sphincter. In phase I, the sphincter and bulb diameters held steady, while the PA and 1st order capillary diameter gradually declined. After ~15 min (phase II), both the sphincter and bulb starts to collapse. After ~25min (phase III), the sphincter is collapsed and only the PA shows continuing decline. * indicates a slope of the linear regression significantly different from zero, n = 3-7 mice. **d**, Estimates of changes in flow resistance within the sphincter using Poiseuille's law at baseline, in phase I, and in phase III.

Discussion

The organization of the cortical vasculature simultaneously accommodates enough pressure for proper

perfusion of each cortical layer while preventing the pressure head from inducing tissue damage. Here, we

show that precapillary sphincters exist and that they represent active bottlenecks that are strategically located

at the upper part of the cortex preferentially in larger PAs that branch into large capillaries. This localization

contributes to equalization of perfusion along the length of the PA. In addition, the pressure drop across the

narrow sphincter (~2-5 µm) protects downstream capillaries and brain tissue both under baseline conditions

and during functional stimulation (Fig. 2-4). However, the high sensitivity of flow resistance to constriction

becomes precarious in pathological conditions that promote general constriction (Fig. 5-6).

The precapillary sphincter equalizes perfusion along the PA and protects

downstream tissue against adverse pressure spikes.

Precapillary sphincters abound at proximal branches of relatively large PAs descending to relatively large 1st

order capillaries, primarily in upper cortical layers (Fig. 2), i.e. in the cerebral microvessels that withstand

289 the high arterial pressure. The sphincters have high flow resistances and reduce the transmural pressure in

290 downstream capillaries, protecting the endothelium from disruption, and contributes to equalize perfusion to

291 all capillary networks along the entire length of the PA. The sphincter location is consistent with the

292 assumption that the blood pressure drop at 1st order capillaries is largest at superficial layers and decrease

293 over the depth of the cortex[25]. Precapillary sphincters represent a bottleneck that may protect the capillary

294 networks from mechanical impact while at the same time preserving the perfusion pressure in the penetrating

295 arteriole along the entire cortical depth. Our data are consistent with studies from other groups which

296 indicate that regulation of capillary blood flow can occur independently from arteriolar flow control[2,26,27].

297 **The distention at the bulb decelerates RBCs, possibly providing a mechanism of**
298 **RBC alignment in capillaries**

299 The bulb, i.e. the distention that usually appeared immediately downstream from the precapillary sphincter

300 (Fig. 1), had areas lacking NG2-expression (Extended data Fig. 4 and Supplementary video 2) which may

301 indicate sparse pericyte coverage. Similar to previous observations[28], we consistently observed short and

302 thick endothelial nuclei at the bulb (Extended data Fig. 4 and Supplementary video 2). The bulb remained

303 less vasoactive compared to the precapillary sphincter and 1st order capillary, consistent with less contractile

304 cell coverage (Fig. 1a, Extended data Fig. 4 and Supplementary video 2). The large cross-sectional area of

305 the bulb caused deceleration and deformation of RBCs from a bullet to parachute form[29] (Supplementary

306 video 5) followed by realignment as RBCs entered the capillary network.

307 **The precapillary sphincter is a highly active flow regulator but remains limited by**
308 **passive structural elements**

309 Our initial analysis of the sphincter complexes suggested a dual role: first, in distributing pressure and

310 perfusion along the PA and second by protecting brain tissue and downstream capillaries against adverse

311 pressures and hemorrhage. In principle, these functions might arise from both active contractile elements and

312 passive structural elements. α-SMA protein is key for contractile function and is widely expressed in

313 vascular smooth muscle and routinely found in pericytes of 1st order capillaries within cortex[14,15,30]. In accord

314 with previous data[31], we observed α-SMA along both the PA and 1st-4th order capillaries and importantly,

315 within the pericyte constituting the sphincter (Fig. 3a). The presence of α-SMA explains the capacity for

316 active vasomotor responses at the sphincter (Fig. 3c-i). The integrity and morphology of the sphincter

317 remained preserved after local administration of papaverine despite a significantly larger dilation for the

318 sphincter as compared to the bulb and 1st order capillary (Fig. 4c)[20]. We report elastin[20] (Fig. 4e, Alexa 633

319 hydrazide) and filamentous collagen α1 type 1 (Fig. 4f, COL1A1) expression that may support the structural

320 integrity of the sphincter during rises in blood pressure (Fig. 4d,e). The high capacity for diameter variations

321 at the sphincter during functional stimulation suggests that cortical flow control resides both in capillaries

322 and at arteriole branchpoints and may reconcile some of the controversies regarding the dynamic regulation

323 of cerebrovascular resistance as described previously[2,15,30,32]. Sphincters are located at proximal PA branches

324 and their occurrence suggests that regulation of cerebral blood is distributed between arterioles and

325 capillaries depending on the local angioarchitecture (Fig. 2). It follows, that the distribution of flow

326 resistance may shift dynamically with changes in perfusion demand[33–35] (Fig. 3). Furthermore, during

327 functional sphincter dilation only one RBC at a time passed into the bulb and 1st order capillary, which

328 suggests that sphincters contribute to plasma skimming[36,37], and thereby contribute to redistribution of RBCs

329 and (in consequence) of hematocrit within the local vascular network.

The precapillary sphincter is vulnerable to pathological conditions of general constriction

332 Cortical spreading depression (CSD) is a slow depolarizing wave along the cortex that is involved in

333 migraine, traumatic brain injury, and stroke[38]. CSD evokes an initial vasoconstriction (phase I), immediately

334 followed by a transient hyperemic response (phase II), which is superseded by a long lasting vasoconstriction

335 of arterioles and capillaries (phase III) during which the neurovascular coupling is impaired[4,39]. During a

336 CSD, the sphincter displayed pronounced diameter changes (Fig. 5) and constricted persistently during the

337 long period of low blood flow after CSD (Supplementary video 6). Persistent sphincter constriction reduced

338 both the RBC flow rate and the hematocrit of the capillary bed. The long lasting oligemia previously

339 described in CSD could arise from the high resistance observed at precapillary sphincters[4], and further

340 pharmacological research on this structure could improve help the outcome of CSD in the ischemic brain or

341   in migraine patient. We also examined the reaction of sphincters to cardiac arrest (Fig. 6). We have

342   previously shown that cerebral pericytes during simulated global ischemia immediately begins to constrict

343   and later starts dying in rigor after ~15 min in rat cortical brain slices[2] (all pericytes lost after ~40min).

344   During *in vivo* imaging of cardiac arrest, we observed a steady vasoconstriction of the precapillary sphincters

345   around 16 min after onset of cardiac arrest (Fig. 6c) and collapse at ~25 min. The other vessel segments

346   displayed linear diameter reductions but no collapse. During global ischemia, we also observed swelling of

347   astrocyte end-feet and soma, which are known to compress microvessels[40], probably adding to the sphincter

348   collapse (Supplementary video 7).

Conclusions

349

350

351   Precapillary sphincters represent important anatomical sites of blood flow regulation due to their strategic

352   placement at branchpoints of proximal PA's, where they control perfusion along the PA. We show that while

353   maximal dilation of the sphincter pericyte is structurally limited, it displays a high capacity of vasomotor

354   activity around a baseline diameter of 3-4 µm, where flow resistance is most sensitive to diameter changes.

355   Therefore, precapillary sphincters represent a mechanism to equalize pressure and RBC flux between the

356   capillary networks that branch off from the upper, middle, and lower parts of the PA. At the same time,

357   sphincters protect downstream capillaries and brain tissue against adverse blood pressure spikes. The dual

358   function is crucial for proper perfusion of cortical vessels. During pathology, sphincter constriction severely

359   limits perfusion of downstream capillaries in CSD and prolonged ischemia. Prevention of sphincter

360   constriction may be of therapeutic importance in migraine and cerebral ischemia.

361

362

Methods

364   *Animal Handling*

365   Animal procedures were approved by The Danish National Ethics committee according to the guidelines set

366   forth in the European Council's Convention for the Protection of Vertebrate Animals Used for Experimental

367 and Other Scientific Purposes. 32 male or female NG2-dsRed mice (Tg(Cspg4-DsRed.T1)1Akik/J; Jackson

368 Laboratory; 19 to 60 weeks old) and 27 male or female wild-type mice (C57bl/6j; Janvier-labs, France;16 to

369 32 week) were used. The NG2-DsRed mice were used in the studies of whisker pad stimulation, cardiac

370 arrest, thinned skull and local ejection of papaverine. The rest of the studies were performed in wild-type

371 mice.

372

373 *Surgical Procedures*

374 Anesthesia was induced with bolus injections of xylazine (10mg/kg, intraperitoneally (i.p.)) and ketamine

375 (60 mg/kg, i.p.) and maintained during surgery with supplemental doses of ketamine (30mg/kg/20 min, i.p.).

376 Mechanical ventilation (Harvard Apparatus, Minivent type 845) was controlled through a cannulation of the

377 trachea. One catheter was inserted in the left femoral artery to monitor blood pressure and to collect blood

378 samples. Another cathether was inserted in the femoral vein to administer chemical compounds. The content

379 of blood gasses in arterial blood samples (50 µl) was analyzed by an ABL700 (Radiometer, Copenhagen;

380 pO2, normal range: 95–110 mmHg; pCO2, normal range: 35–40 mmHg; pH, normal range: 7.35–7.45). To

381 maintain physiological conditions, both respiration and mixed air supply was adjusted according to the blood

382 gas analysis or occasionally according to continuously monitored end-expiratory CO_2 (Harvard Apparatus,

383 Capnograph 340), blood oxygen saturation (Kent Scientific, MouseStat pulsoximeter). A craniotomy

384 (diameter ~3 mm. Center coordinates: 3 mm right of and 0.5 mm behind bregma) was drilled above the right

385 somatosensory barrel cortex. We switched anesthesia to α-chloralose (33% w/vol; 0.01 mL/10 g/h) upon

386 surgery completion. In the end of the experiments, mice were euthanized by intravenous injection of

387 pentobarbital followed by cervical dislocation.

388 To ensure that precapillary sphincters were not a result of the craniotomy, we made thinned skull

389 preparations over the barrel cortex, at the point of the surgical procedure where we would otherwise have

390 made a craniotomy. By following the protocol by Shih et al[41], we thinned the skull to around 40 µm

391 thickness, polished with tin oxide powder and covered the window with agarose and a coverslip.

392

Chronic cranial window implantation

A chronic cranial window was installed approximately three weeks prior to imaging in mice of a C57Bl/6 background. The surgical procedure is adapted from Goldey et al.[42]. A small craniotomy was performed over the left barrel cortex under isoflurane anaesthesia and a custom-made reinforced cover glass consisting of three 3 mm coverslips glued on top of each other and onto a 5 mm coverslip was installed. A custom-made head bar was attached to the right side of the skull allowing for head immobilization during imaging sessions. In the five days following implantation the animal was closely monitored and given pain and infection treatment as described in Goldey et al.[42]. When the animal had recovered after surgery, training for imaging experiments could commence. The animal was familiarized with the experimenter through gentle handling. After several handling sessions and when the animal was comfortable with the experimenter, it was slowly accustomed to head immobilization. The animal was given treats in form of sweetened condensed milk during the training process. When the animal had been habituated with the head immobilization for periods of about an hour of length, they are ready for imaging experiments.

Electrical stimulation in whisker pad

The mouse sensory barrel cortex was activated by whisker pad stimulation. The contralateral ramus infraorbitalis of the trigeminal nerve was electrically stimulated using a set of custom-made bipolar electrodes inserted percutaneously. The cathode was positioned relative to the hiatus infraorbitalis (IO), and the anode was inserted into the masticatory muscles. Thalamocortical IO stimulation was performed at an intensity of 1.5 mA (ISO-flex; A.M.P.I.) for 1 ms in trains of 20 s at 2 Hz.

Pressure ejection of papaverine via glass micro-pipette

415   Borosilicate glass micro-pipettes were produced by a pipette puller (P-97, Sutter Instrument) with a

416   resistance of 2.5 ~ 3.0 MΩ. The pipette was loaded with a mixture of 10 μM Alexa 594 and 10 mM

417   papaverine in order to visualize the pipette tip in both epi-fluorescent camera and two-photon microscope.

418   Guided by the two-photon microscopy and operated by a micromanipulator, the pipette was carefully

419   inserted into the cortex to minimize tissue damage and avoid vessel bleeding. The distance between the

420   pipette tip and vasculature was 30-50 µm. Papaverine was locally ejected for ~1 s by 3 times using an air

421   pressure of <15 psi in the pipette (PV830 Pneumatic PicoPump, World Precision Instruments). A red cloud

422   (Alexa 594) ejected from the pipette tip was visually observed to cover the local vascular region

423   simutaneously, and the background returned to normal approximately 1 minute after puffing[3]. Papaverine

424   was pre-conditioned for 5 minutes before imaging the same vasculature again.

425

426   *Cortical Spreading Depression*

427   In a subset of experiments, cortical spreading depolarization (CSD) was triggered 2 mm away from the

428   recording site using pressure injection of 0.5 M potassium acetate (KAc) into the cortex (estimated volume

429   ~0.5 μl). Apart from triggering CSD, KAc injection did not cause a brain lesion (bleeding or tissue damage),

430   and to ensure that no spreading depolarization was triggered during surgical preparation, our technique for

431   making craniotomies has previously been validated by measuring cerebral blood flow while drilling the

432   craniotomy. Using this technic, we could show that no spreading depolarization was elicited[39]. Moreover,

433   prior to our first spreading depolarization we measure whisker responses, and mice that did not show normal

434   vessel diameter responses to stimulation were discarded from the dataset, ensuring that no spreading

435   depolarization were triggered before recordings started.

436

437   *Two-photon imaging*

438   Images and videos were obtained using two sets of laser-scanning two-photon microscopes. Experiments of

439   prevalence quantification, RBC velocity, evoked Ca^{2+} responses, CSD, and cardiac arrest were performed

440   using a commercial two-photon microscope (FluoView FVMPE-RS, Olympus) equipped with a 25 x1.05

441   NA-water-immersion objective (Olympus) and a Mai Tai HP Ti:Sapphire laser (Millennia Pro, Spectra

442   Physics). Experiments of whisker pad stimulation and papaverine ejection were performed using a second

443   commercial two-photon microscope (Femto3D-RC, Femtonics Ltd.) with a 25×1.0 NA water-immersion

444   objective with piezo motor and a Ti:Sapphire laser, Mai Tai HP Deep See, Spectra-Physics. The excitation

445   wavelength was set to 900 nm. The emitted light was filtered to collect red (590-650nm) and green (510-

446   560nm) light from dsRed (pericytes) or SR101 (astrocytes) and FITC-dextran (vessel lumen) or OGB

447   (relative Ca^{2+} changes), respectively.

448   The prevalence of precapillary sphincters and bulbs were studied by acquiring image stacks using our

449   Olympus two-photon microscope (Fluoview), tracking each penetrating arteriole from pial to >650 µm in

450   depth in a frame-scan mode at around 1 frame per second with pixel resolution of 512x512 at 1000 nm

451   excitation wavelength. Measurements of RBC velocity were performed in resonance bi-directional line-scan

452   mode with a scan rate of 15,873 Hz (0.063 ms per line) and pixel resolution of 512 pixels per line. Evoked

453   Ca^{2+} responses and CSD was imaged in one vessel branching from the penetrating arteriole to a first order

454   capillary, including the neck and bulb structure in a single plane. Evoked Ca^{2+} responses and CSD's was

455   imaged in one vessel branching from the penetrating arteriole to a first order capillary, including the neck

456   and bulb structure in a single plane. The excitation wavelength was set to 900, the frame resolution was

457   0.450 μm/pixel with a 320 x 240 pixels frame and images were taken at a speed of 2.40 frames per second

458   for evoked Ca^{2+} responses. The excitation wavelength was set to 920 nm, the frame resolution was 0.255

459   μm/pixel with a 512 x 384 pixels frame and images were taken at a speed of 0.81 frames per second for

460   CSD.

461   In the experiments using Femtonics microscope, we recorded the whole volume including the vessel

462   segments of interest by fast repetitive hyperstack imaging (4D imaging) - continuous cycles of image stacks

463   along the z-axis. This is to compensate focus drift and study vasculatures spanning in a certain z-axis range.

464   Each image stack was acquired within 1 second that comprised 9-10 planes with a plane distance of 3 - 4

465   µm. This covered the whole z-axis range of the investigated blood vessels. The pixel sizes in the x-y plane

466   were 0.2 - 0.3 µm.

467

468   *Two-photon imaging analysis*

469   Data were analyzed in ImageJ or MATLAB using custom-built software. In the study of prevalence of

470   precapillary sphincters and cardiac arrest, multiple ROIs were manually placed across vessel lumen in

471   ImageJ, measuring vessel diameters. In the study of whisker pad stimulation induced evoked Ca^{2+} responses,

472   ROIs were detected using a modification of the pixel-of-interest-based analysis method[43]. ROIs were

473   positioned around astrocytic end-feet and labeled according to their location on PA, sphincter or 1st order

474   capillary. Further ROIs were positioned around neuronal somas and in neuropil. Astrocytic or neuronal

475   structures were recognized based on SR101/OGB staining, cell morphology, and relation to blood vessels[44].

476   For each frame, we selected pixels showing intensities of 1.5 standard deviations (SD) above the mean

477   intensity of the ROI. The intensities of these pixels were averaged and then normalized to a 15-s baseline

478   period just before stimulation onset, creating a time trace of $\Delta F/F_0$ for every ROI. These time traces were

479   smoothed with a 3-sec moving average to avoid outlier values. A Ca^{2+} transient was defined as an intensity

480   increase of ≥5% and of ≥2 SD from baseline, having a duration of ≥2.5 s. Recordings were divided into 20-s

481   time bins (baseline, dilation, undershoot). Responsivity was defined as the fraction of ROIs with Ca^{2+}

482   transients within time bins per mouse. Recordings lacking evoked Ca^{2+} responses in neuropil were excluded

483   from analysis. In the study of CSD, rectangular region of interests (ROIs) with width of 2 or 4 µm were

484   drawn perpendicular to the surface of the vessel at the defined locations. An active contour algorithm (Chan-

485   Vese segmentation) was used to calculate the vessel diameter change in these ROIs. The diameter change

486   over time was detected for each ROI. For the 4D imaging performed in whisker pad stimulation and

487   papaverine ejection, each image stack was flattened onto one image by maximal intensity projection, which

488   converts the data to the same formats of CSD. Similar diameter analysis methods were used. Values from

489   each ROI type were averaged per mouse. Arteriole bifurcations leading to two equally sized arterioles and 1st

490 order capillaries bifurcating under 10 µm from the arteriole branchpoint were not included in the analysis.

491 3D renderings for supplementary videos were done with Amira software (ThermoFischer scientific).

492

493 *Immunohistochemistry*

494 Adult NG2-ds-Red mice were transcardially perfused with 4% paraformaldehyde (PFA) and their brains

495 were extracted and cryoprotected in 30% sucrose, rapidly frozen in cold isopenthane (-30°C) and sectioned

496 using cryostat at 25 and 50 µm thickness. Sections were rinsed (3 x 5 min) in 0.1 M PBS and antigen retrival

497 was performed (for Collagen-I staining) using hot citrate buffer (90°C, pH 6.0) for 20 minutes. 50 µm

498 sections were permeabilized and blocked in 0.5% Triton-X 100 in 1 X PBS (pH 7.2) and 1% BSA overnight

499 at 4°C, whereas 25 µm sections were permeabilized in 0.5% Triton-X 100 in 1 X PBS for 30 minutes and

500 blocked in 5% NGS, 5% BSA and 0.5% Triton-X 100 in 1 X PBS for 1 hour at RT. Sections were incubated

501 in primary antibodies for two nights at 4°C in blocking buffer containing 1-5% BSA, 5% NGS in 0.25-0.5%

502 Triton-X 100 in 1 X PBS. The following primary antibodies were used: mouse ACTA2-FITC (1:200; Sigma;

503 F3777) and rabbit anti-Collagen I (1:50; ab34710). Elastin was labeled using an artery-specific red dye;

504 Alexa Fluor 633 (A30634, ThermoFisher Scientific) at 1:300 dilution from 2mM stock. Alexa Fluor 633 was

505 added to the brain sections for 10 minutes and rinsed. Thereafter, the sections were washed (3 x 5 min) in 0.1

506 M PBS and incubated with goat anti-rabbit Alexa488 (1:500; Sigma-Aldrich) secondary antibody (to label

507 collagen-I) for 1 hour at RT. After incubation with secondary antibody sections were rinsed (3 x 5 min) in

508 1X PBS, incubated in Hoechst (1: 6000) for 7 minutes, rinsed again (3 x 5 min) in 1X PBS and mounted

509 using SlowFade^TM Diamond Antifade Mountant (Invitrogen; S36963). Fluorescence images were acquired

510 with a confocal laser scanning microscope (LSM 700 or 710) equipped with Zen software at 20x/0.8 NA and

511 63x/1.40 NA oil DIC M27 objectives, 1X (0.170 µm/pixel) and 4X (0.021 µm/pixel) digital zoom

512 respectively. Care was taken to ensure similar fluorescence across images.

513

514 *Statistical analysis*

515 Datasets are presented as mean ± s.e.m, standard box plots, or in case of log-transformed data as back-

516 transformed means ± 95% confidence intervals. Normality of data was assessed using Shapiro-Wilk and

517 graphical tests. For normal datasets, Linear Mixed Effects (LME) model analyses were performed. LME was

518 chosen to take proper advantage of multiple measurements of parameters and/or of multiple time points in

519 the same animal. Vessel segments (PA, sphincter, bulb, and 1st order capillary) were included as the fixed

520 effect, whereas the particular mouse and vessel branch were included as random effects as needed.

521 Heteroscedastic datasets were log-transformed to conform to analysis as indicated. Significant difference (p-

522 value < 0.05) was obtained by likelihood ratio tests of the LME model with the fixed effect in question

523 against a model without the fixed effect. Tukeys post-hoc test was used for pairwise comparisons between

524 elements in the fixed effect group. For non-normal data, non-parametric Wilcoxon signed-rank tests were

525 used for paired samples, while the Kruskal-Wallis test was used for multiple independent groups; for

526 pairwise comparisons, the Wilcoxon rank-sum test with Holm's p-value adjustment method was used.

527 Finally, linear regression was used to assess the relationships were fitted to datasets. All statistical analysis

528 was conducted using R (version 3.4.4; packages *lme4*[45] and dplyr) and Prism version 5.

529

Acknowledgements

536

References

538 1. Attwell, D. *et al.* Glial and neuronal control of brain blood flow. *Nature* **468**, 232–243 (2010).

539   2. Hall, C. N. *et al.* Capillary pericytes regulate cerebral blood flow in health and disease. *Nature* **508**, 55–60

540   (2014).

541   3. Cai, C. *et al.* Stimulation-induced increases in cerebral blood flow and local capillary vasoconstriction

542   depend on conducted vascular responses. *Proc. Natl. Acad. Sci. U. S. A.* **115**, E5796–E5804 (2018).

543   4. Khennouf, L. *et al.* Active role of capillary pericytes during stimulation-induced activity and spreading

544   depolarization. *Brain J. Neurol.* **141**, 2032–2046 (2018).

545   5. Rungta, R. L., Chaigneau, E., Osmanski, B.-F. & Charpak, S. Vascular Compartmentalization of

546   Functional Hyperemia from the Synapse to the Pia. *Neuron* **99**, 362–375.e4 (2018).

547   6. Duvernoy, H. M., Delon, S. & Vannson, J. L. Cortical blood vessels of the human brain. *Brain Res. Bull.*

548   **7**, 519–579 (1981).

549   7. Chambers, R. & Zweifach, B. W. Functional Activity of the Blood Capillary Bed, with Special Reference

550   to Visceral Tissue. *Ann. N. Y. Acad. Sci.* **46**, 683–695 (1946).

551   8. Altura, B. M. Chemical and humoral regulation of blood flow through the precapillary sphincter.

552   *Microvasc. Res.* **3**, 361–384 (1971).

553   9. Harris, P. D. & Longnecker, D. E. Significance of precapillary sphincter activity for microcirculatory

554   function. *Microvasc. Res.* **3**, 385–395 (1971).

555   10.   Chambers, R. & Zweifach, B. W. Topography and function of the mesenteric capillary

556   circulation. *Am. J. Anat.* **75**, 173–205 (1944).

557   11.   Sakai, T. & Hosoyamada, Y. Are the precapillary sphincters and metarterioles universal

558   components of the microcirculation? An historical review. *J. Physiol. Sci.* **63**, 319–331 (2013).

559   12.   Ushiwata, I. & Ushiki, T. Cytoarchitecture of the smooth muscles and pericytes of rat cerebral

560   blood vessels. *J. Neurosurg.* **73**, 82–90 (1990).

561   13.   Armulik, A., Genové, G. & Betsholtz, C. Pericytes: Developmental, Physiological, and

562   Pathological Perspectives, Problems, and Promises. *Dev. Cell* **21**, 193–215 (2011).

563   14.   Hartmann, D. A. *et al.* Pericyte structure and distribution in the cerebral cortex revealed by

564   high-resolution imaging of transgenic mice. *Neurophotonics* **2**, 041402 (2015).

565 15.   Grant, R. I. *et al.* Organizational Hierarchy and Structural Diversity of Microvascular

566   Pericytes in Adult Mouse Cortex. *bioRxiv* 114777 (2017). doi:10.1101/114777

567 16.   Bekar, L. K., Wei, H. S. & Nedergaard, M. The locus coeruleus-norepinephrine network

568   optimizes coupling of cerebral blood volume with oxygen demand. *J. Cereb. Blood Flow Metab. Off. J.*

569   *Int. Soc. Cereb. Blood Flow Metab.* **32**, 2135–2145 (2012).

570 17.   Harris, D. E. & Warshaw, D. M. Length vs. active force relationship in single isolated smooth

571   muscle cells. *Am. J. Physiol.* **260**, C1104-1112 (1991).

572 18.   Boswell-Smith, V., Spina, D. & Page, C. P. Phosphodiesterase inhibitors. *Br. J. Pharmacol.*

573   **147 Suppl 1**, S252-257 (2006).

574 19.   Bolton, T. B. Mechanisms of action of transmitters and other substances on smooth muscle.

575   *Physiol. Rev.* **59**, 606–718 (1979).

576 20.   Shen, Z., Lu, Z., Chhatbar, P. Y., O'Herron, P. & Kara, P. An artery-specific fluorescent dye

577   for studying neurovascular coupling. *Nat. Methods* **9**, 273–276 (2012).

578 21.   Piilgaard, H. & Lauritzen, M. Persistent increase in oxygen consumption and impaired

579   neurovascular coupling after spreading depression in rat neocortex. *J. Cereb. Blood Flow Metab. Off. J.*

580   *Int. Soc. Cereb. Blood Flow Metab.* **29**, 1517–1527 (2009).

581 22.   Nakai, K. *et al.* Microangioarchitecture of rat parietal cortex with special reference to vascular

582   'sphincters'. Scanning electron microscopic and dark field microscopic study. *Stroke* **12**, 653–659 (1981).

583 23.   Anderson, B. G. & Anderson, W. D. Scanning electron microscopy of microcorrosion casts;

584   intracranial and abdominal microvasculature in domestic animals. *Am. J. Anat.* **153**, 523–536 (1978).

585 24.   Harrison, R. V., Harel, N., Panesar, J. & Mount, R. J. Blood capillary distribution correlates

586   with hemodynamic-based functional imaging in cerebral cortex. *undefined* (2002). Available at:

587   /paper/Blood-capillary-distribution-correlates-with-in-Harrison-

588   Harel/4ef687b8863827c6db73e1ea69cfe9d055957150. (Accessed: 11th September 2018)

589 25.   Schmid, F., Tsai, P. S., Kleinfeld, D., Jenny, P. & Weber, B. Depth-dependent flow and

590   pressure characteristics in cortical microvascular networks. *PLoS Comput. Biol.* **13**, (2017).

591 26.   Mishra, A. *et al.* Astrocytes mediate neurovascular signaling to capillary pericytes but not to

592   arterioles. *Nat. Neurosci.* **19**, 1619–1627 (2016).

593 27.   Blinder, P. *et al.* The cortical angiome: an interconnected vascular network with noncolumnar

594   patterns of blood flow. *Nat. Neurosci.* **16**, 889–897 (2013).

595 28.   Rhodin, J. A. The ultrastructure of mammalian arterioles and precapillary sphincters. *J.*

596   *Ultrastruct. Res.* **18**, 181–223 (1967).

597 29.   Tomaiuolo, G., Lanotte, L., D'Apolito, R., Cassinese, A. & Guido, S. Microconfined flow

598   behavior of red blood cells. *Med. Eng. Phys.* **38**, 11–16 (2016).

599 30.   Hill, R. A. *et al.* Regional blood flow in the normal and ischemic brain is controlled by

600   arteriolar smooth muscle cell contractility and not by capillary pericytes. *Neuron* **87**, 95–110 (2015).

601 31.   Grant, R. I. *et al.* Organizational hierarchy and structural diversity of microvascular pericytes

602   in adult mouse cortex. *J. Cereb. Blood Flow Metab.* **39**, 411–425 (2019).

603 32.   Peppiatt, C. M., Howarth, C., Mobbs, P. & Attwell, D. Bidirectional control of CNS capillary

604   diameter by pericytes. *Nature* **443**, 700–704 (2006).

605 33.   Welsh, D. G. & Longden, T. A. Endothelial signaling and the dynamic regulation of arterial

606   tone: A surreptitious relationship. *Microcirc. N. Y. N 1994* **24**, (2017).

607 34.   Iadecola, C. The Neurovascular Unit Coming of Age: A Journey through Neurovascular

608   Coupling in Health and Disease. *Neuron* **96**, 17–42 (2017).

609 35.   Longden, T. A. & Nelson, M. T. Vascular inward rectifier K+ channels as external K+ sensors

610   in the control of cerebral blood flow. *Microcirc. N. Y. N 1994* **22**, 183–196 (2015).

611 36.   Pries, A. R., Ley, K., Claassen, M. & Gaehtgens, P. Red cell distribution at microvascular

612   bifurcations. *Microvasc. Res.* **38**, 81–101 (1989).

613 37.   Pries, A. R. & Secomb, T. W. Microvascular blood viscosity in vivo and the endothelial

614   surface layer. *Am. J. Physiol.-Heart Circ. Physiol.* **289**, H2657–H2664 (2005).

615 38.   Lauritzen, M. *et al.* Clinical relevance of cortical spreading depression in neurological

616   disorders: migraine, malignant stroke, subarachnoid and intracranial hemorrhage, and traumatic brain

617   injury. *J. Cereb. Blood Flow Metab.* **31**, 17–35 (2011).

618   39.   Khennouf, L., Gesslein, B., Lind, B. L., van den Maagdenberg, A. M. J. M. & Lauritzen, M.

619   Activity-dependent calcium, oxygen, and vascular responses in a mouse model of familial hemiplegic

620   migraine type 1. *Ann. Neurol.* **80**, 219–232 (2016).

621   40.   Ito, U., Hakamata, Y., Kawakami, E. & Oyanagi, K. Temporary focal cerebral ischemia

622   results in swollen astrocytic end-feet that compress microvessels and lead to focal cortical infarction. *J.*

623   *Cereb. Blood Flow Metab.* **31**, 328–338 (2011).

624   41.   Shih, A. Y., Mateo, C., Drew, P. J., Tsai, P. S. & Kleinfeld, D. A Polished and Reinforced

625   Thinned-skull Window for Long-term Imaging of the Mouse Brain. *J. Vis. Exp. JoVE* (2012).

626   doi:10.3791/3742

627   42.   Goldey, G. J. *et al.* Removable cranial windows for long-term imaging in awake mice. *Nat.*

628   *Protoc.* **9**, 2515–2538 (2014).

629   43.   Lind, B. L. *et al.* Fast Ca2+ responses in astrocyte end-feet and neurovascular coupling in

630   mice. *Glia* **66**, 348–358 (2018).

631   44.   Fordsmann, J. C. *et al.* Spontaneous astrocytic Ca2+ activity abounds in electrically

632   suppressed ischemic penumbra of aged mice. *Glia* **67**, 37–52 (2019).

633   45.   Thomsen, K. *et al.* Initial brain aging: heterogeneity of mitochondrial size is associated with

634   decline in complex I-linked respiration in cortex and hippocampus. *Neurobiol. Aging* **61**, 215–224 (2018).

635

636